The following publication L. Lei et al., "Toward Lung Ultrasound Automation: Fully Autonomous Robotic Longitudinal and Transverse Scans Along Intercostal Spaces," in IEEE Transactions on Medical Robotics and Bionics, vol. 7, no. 2, pp. 768-781, May 2025 is available at https://doi.org/10.1109/TMRB.2025.3550663.

Towards Lung Ultrasound Automation: Fully Autonomous Robotic Longitudinal and Transverse Scans Along Intercostal Spaces

Long Lei*, Yingbai Hu*, Zixing Jiang*, Juzheng Miao, Xiao Luo, Yu Zhang, Qiong Wang, Shujun Wang†, Zheng Li†, Pheng-Ann Heng

***Abstract*—Lung ultrasound scanning is essential for diagnosing lung diseases. The scan effectiveness critically depends on both longitudinal and transverse scans through intercostal spaces to reduce rib shadowing interference, as well as maintaining the probe perpendicular to pleura for pathological artifact generation. However, achieving this level of scan quality often depends heavily on the experience of doctors. In this paper, we present an advance scanning method that towards full autonomy in lung ultrasound operations, focusing on longitudinal and transverse scans. We address the unique characteristics of lung ultrasound scanning by developing path planning methods along intercostal spaces and solving adaptive probe posture adjustment using real-time pleural line feedback. This ensures the acquisition of high-quality, diagnostically meaningful ultrasound images. Moreover, we develop a robotic lung ultrasound system to validate the proposed methods. Extensive experimental results on a volunteer and a chest phantom confirm the efficacy of our methods, and demonstrate the system's effectiveness in performing automated lung ultrasound examinations. Our work is pioneering in enabling robotic lung ultrasound scanning to autonomously navigate intercostal spaces and optimize probe posture.**

***Index Terms*—robotic ultrasound system, lung ultrasound, medical automation**

I. Introduction

LUNG Ultrasound (LUS) allows doctors to safely and quickly obtain immediate images of a patient's lungs. It has been shown to be superior to bedside chest X-rays and comparable to chest CT in diagnosing various pleural and pulmonary conditions, such as pediatric pneumonia [1] and COVID-19 [2] [3]. Compared to CT scans or chest X-rays, ultrasound equipment is generally more affordable, portable, and user-friendly, enabling rapid bedside evaluations. This is particularly valuable in emergency, critical care, and resource-limited settings, such as remote or rural areas. Moreover, lung ultrasound does not carry the risk of ionizing radiation, making it suitable for repeated use, especially in pregnant women, children, and critically patients who require frequent monitoring [4]. Lung ultrasound examination requires both longitudinal and transverse scans along intercostal spaces for each hemithorax [5], as shown in Fig. 1. To obtain adequate ultrasound image samples through the intercostal spaces for diagnosis, these images are unobstructed or minimally disturbed by ribs. Unlike the ultrasound examinations for other organs, a diseased lung is primarily identified from a healthy lung through artifacts including A-lines and B-lines [6]. A-lines are several hyperechoic lines parallel to a pleural line,

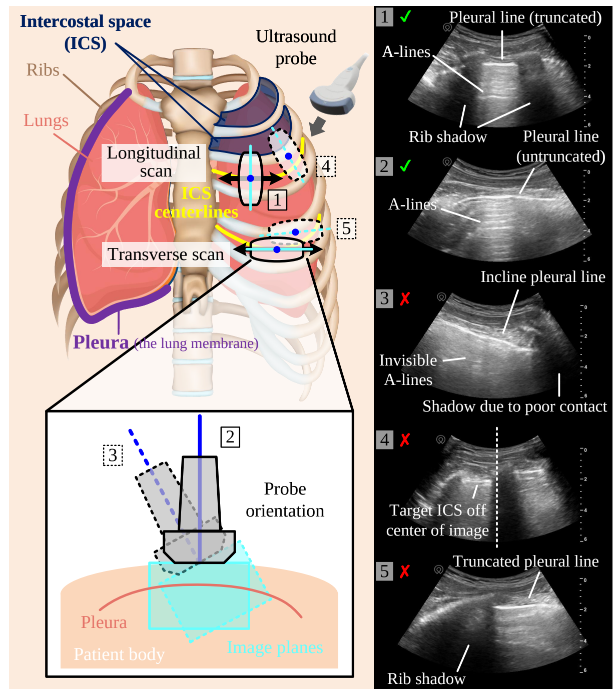

Fig. 1. Illustration of lung ultrasound scan protocol. Lung ultrasound examination requires both longitudinal and transverse scans along the intercostal spaces, with the probe maintained perpendicular to the pleural.

This work was supported in part by the Research Grants Council of the Hong Kong Special Administrative Region, China (Project No.: T45-401/22-N), in part by the Hong Kong Innovation and Technology Fund under Grant GHP/080/20SZ. (**Long Lei, Yingbai Hu, and Zixing Jiang contributed equally to this work.* †*Corresponding authors: Shujun Wang, Zheng Li.*)

Long Lei, Juzheng Miao, Yu Zhang, and Pheng-Ann Heng are with Department of Computer Science and Engineering, The Chinese University of Hong Kong, Hong Kong, China. (e-mail: longlei@cuhk.edu.hk; jzmiao22@cse.cuhk.edu.hk; yzhang@cuhk.edu.hk; pheng@cse.cuhk.edu.hk).

Yingbai Hu is with Multi-scale Medical Robotics Centre Ltd., The Chinese University of Hong Kong, Hong Kong, China. (e-mail: yingbaihu@mrc-cuhk.com).

Zixing Jiang and Xiao Luo are with Department of Surgery, The Chinese University of Hong Kong, Hong Kong, China. (e-mail: zxjiang@surgery.cuhk.edu.hk; xluo@surgery.cuhk.edu.hk).

Qiong Wang is with Shenzhen Institute of Advanced Technology, Chinese Academy of Sciences, Shenzhen, China. (e-mail: wangqiong@siat.ac.cn).

Shuju Wang is with Department of Biomedical Engineering, The Hong Kong Polytechnic University, Hong Kong, China. (e-mail: shu-jun.wang@polyu.edu.hk).

Zheng Li is with Department of Surgery, Chow Yuk Ho Technology Centre for Innovative Medicine, Li Ka Shing Institute of Health Sciences, and Multiscale Medical Robotics Centre Ltd., The Chinese University of Hong Kong, Hong Kong, China. (e-mail: lizheng@cuhk.edu.hk).

they are normal lung ultrasound sign. When the lung tissue becomes diseased and the gas in the lung is partially replaced by substances that can conduct ultrasonic waves, such as exudate and blood, ultrasound waves can reach deeper tissues and form a hyperechoic beam perpendicular to the pleural line, called the B-lines. These A-lines and B-lines can only be fully produced when the ultrasound pulses are emitted vertically onto the pleura [7], [8], allowing the probe to receive the strongest echoes from the pleura. Therefore, maintaining the probe perpendicular to the pleura is essential to acquire diagnostically meaningful ultrasound images.

During a lung ultrasound scan, sonographers or clinicians must apply appropriate pressure with the probe on the patient's chest and move it in specific patterns to examine different parts of the lungs for potential pathologies, diagnosing based on the resulting images [9]. Scanning techniques can vary significantly between doctors, and diagnostic accuracy often depends on their level of experience. Additionally, manual scanning exposes doctors directly to the patient's environment, increasing the risk of infection. Prolonged manual scanning can also lead to muscle fatigue and decreased concentration, which may compromise diagnostic accuracy. An autonomous robotic lung ultrasound system (RLUS) could standardize and automate the scanning process, reducing the physical burden and infection risks for doctors, allowing them to focus on diagnosis [10], [11]. This would benefit both doctors and patients, particularly in remote areas.

In this paper, we focus on achieving full autonomy in the two fundamental operations of lung ultrasound: longitudinal and transverse scans. This represents a significant step toward fully autonomous robotic lung ultrasound scan for the entire lung ultrasound examinations. By addressing the unique characteristics of lung ultrasound, we have developed solutions for path planning along the intercostal spaces for both scan types. Additionally, we also solved the problem of adaptive probe posture adjustment using real-time pleural line feedback. These advancements ensure the acquisition of a sufficient number of high-quality ultrasound images that are diagnostically meaningful. To the best of our knowledge, this is the first work that enables robotic lung ultrasound scanning to automatically follow intercostal spaces while optimizing probe posture based on pleural line feedback. The main contributions of this paper are as follows:

1) We propose a patient-specific lung ultrasound scan path planning method that enables longitudinal scan along the intercostal spaces by extracting intercostal centerlines from a standard human model and adapting them to individual patient surface data. This is the first work that plans lung ultrasound scanning paths along the intercostal spaces.
2) We propose a method for the actual intercostal centerlines location through pleural line segmentation and reconstruction based on the longitudinal scan results, further to plan transverse scan paths, ensuring that the transverse scans obtain ultrasound images unobstructed by ribs.
3) We propose an ultrasound probe posture control method based on real-time pleural line feedback servo for the first time, both eliminating the possibility of the target pleural line deviating from the imaging field of view during the longitudinal scan and ensuring the full generation of pathological artifacts for obtaining diagnostically meaningful ultrasound images during overall scanning process.
4) A robotic lung ultrasound scan system is developed, and the scan workflow is standardized. Experiments conducted on a volunteer and a chest phantom validate the performance of the proposed methods and the system.

The rest of this article is organized as follows. Section II reviews the related works. Section III introduces the system setup and calibration method. Section IV presents the longitudinal scan path planning method. Section V presents the pleural line segmentation from ultrasound images, intercostal centerline reconstruction for transverse scan path planning, online probe posture adjustment, and compliant motion control methods. Section VI presents the experiments and results. Finally, Section VII concludes this article.

II. Related works

A. Robotic Lung Ultrasound Scan System

Existing autonomous robotic lung ultrasound systems can be mainly divided into two categories: Imaging only at several specific locations [12]–[15] and scanning the lung zones along specific trajectories [16]–[18]. The systems of the first type usually follow the 8-point Point-of-Care Ultrasound (POCUS) [19] or Bedside Lung Ultrasound in Emergency (BLUE) [20] protocols, or the 10-point BLUE-plus [21] protocol, and automatically obtain ultrasound images at these positions for diagnosis. Although this method is efficient, the scanning range is limited and there is a risk of missed diagnosis [22]. This issue is particularly highlighted for the COVID-19, where the viral pneumonia is characterized by multiple discrete interstitial B-lines in the lung [2]. When inflammatory lesions do not appear at these specific locations, the missed diagnosis occurs.

Scanning the lung zones can avoid missed diagnoses. Just like the robotic full-coverage ultrasound scan for other organs, such as breast [23], lumbar [24], and abdominal organs [25], this type of RLUS also adopts a two-step workflow [12], [16], [18]. The first step is to plan a scan trajectory consisting of a series of probe positions and attitudes based on the patient's body surface point cloud, which is obtained from preoperative magnetic resonance imaging (MRI) or computed tomography (CT) images [26] or a depth camera. Then, the robot holds the probe and performs ultrasound scan along the planned trajectory. During this process, the probe posture is usually fine-tuned in real time based on the actual contact force and image feedback information, to obtain high-quality ultrasound images and ensure scan security. However, existing RLUS can neither achieve scanning along the intercostal spaces nor consider the impact of probe posture on artifact generation.

B. Ultrasound Scan Path Planning

Currently, various of lung ultrasound scan path planning methods were proposed. Suligoj et al. [16] first divide a plane grid evenly according to the scan boundary and the probe size, and then generates the actual curve scan path by projecting these grid points onto the skin surface. Tan et al. [18] slice the body surface point set at a certain interval along the cranial-caudal direction, and use a 3rd degree nonuniform rational B-splines (NUBRS) curve-fitting method to obtain the scan path. Since these path planning methods do not account for the obstruction of imaging caused by anatomical structures such as ribs, they can result in images that are meaningless for diagnosis [27] and may interfere with the doctor's judgment. Jiang et al. [28] propose a non-rigid registration method between the thoracic cartilage point sets extracted from a CT template and a patient's ultrasound images, to map intercostal scan paths from a generic atlas to the individual patient. However, preliminary ultrasound scan of cartilages is required, which significantly increases the ultrasound scan time.

C. Probe Posture Control

Most of ultrasound scan robots use the normal direction of the skin surface at the contact point as the central axis direction of the probe [12], [13], [16], [23], [24], [29]–[32], which is considered to ensure the optimal acoustic coupling between the transducer and the body, thus providing a clear visualization of pathological clues [33]. Before scan, the skin normal direction is often directly calculated based on the patient's body surface point cloud [13], [16], [23], [24], [29]. During the scan, Jiang et al. [30], [31] identify the normal direction of the body surface based on the change in the contact force between the probe and the tissue during its fan-shaped movement. Ma et al. [12] calculate rotation adjustment values towards perpendicularity based on the distances to the skin sensed by multiple distance sensors installed around the probe. There are also some works that online optimize the probe posture based on the coverage level or imaging angle of the target anatomical structures [27], [34], [35]. jiang et al. [34] align the probe to the normal direction of the target blood vessel to accurately measure its diameter. However, there are differences in the thickness of the fat and muscle layers at different locations in the chest, the normal direction of the body surface is not always perpendicular to the pleura, resulting in possible failure to produce A- and B-lines. Furthermore, no one has yet directly used the pleural lines in ultrasound images as feedback to adjust the probe posture.

III. System Setup and Method Overview

A. System Setup

Based on the need for lung ultrasound scan, we developed a robotic lung ultrasound system, as shown in Fig. 2(a). The hardware of the developed RLUS mainly includes a 6 degree-of-freedom (DoF) lightweight robot (UR5, Universal Robots, Denmark), an ultrasound imaging system (Clover 60, Wisonic, China) with a convex array probe (V5-1, Wisonic, China), a frame grabber (OK_VGA41A-4E+, JoinHope Image, China), a 6-axis force/torque (F/T) sensor (M3733C, Sunrise Instruments, China), an RGB-D camera (RealSense D435i, Intel, USA), and a host computer. The ultrasound probe is connected to the end flange of the robot by a customized fixture via the F/T sensor, and the fixture has a symmetrical structure that can automatically align the axis of the probe,

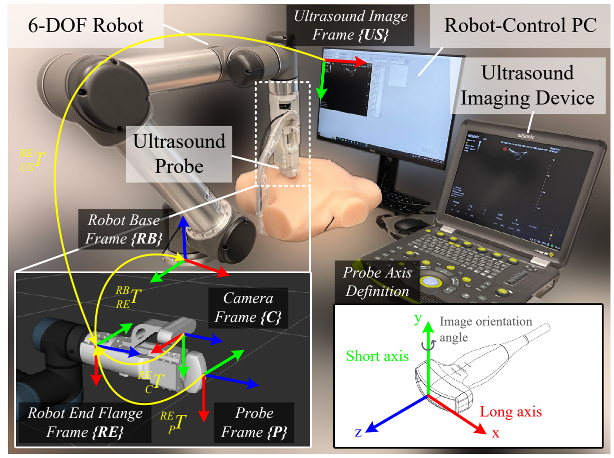

Fig. 2. Robotic lung ultrasound scan system setup and involved coordinate transformations.

sensor and end flange of the robot. The F/T sensor is used to measure the real-time contact force between the probe and the subject's skin. The camera is used to obtain the point cloud of the subject's body surface, which is also fixed at the end of the robot through a 3D printed clamp. The frame grabber is plugged into the host motherboard and used to collect ultrasound images from the ultrasound imaging system through its HDMI port.

The software of the developed robotic system mainly includes two modules: an ultrasound image capture and analysis (USCA) module, and a robot control module. The USCA module is mainly used to continuously capture ultrasound images, segment pleural lines based on a deep learning model, and analyze the pleural line segmentation results. This main program of this module is built with the Qt toolkit (Qt 5.15.2), the deep learning model is deployed as a back-end server with the Flask framework (Flask 2.2.5), and the two parts communicate using the POST method of the HTTP protocol. The robot control module is mainly used for system calibration, obtaining body surface point cloud data, path planning, intercostal centerline reconstruction, and robot motion simulation and control under a hybrid force-position framework. This module is developed with the Robot Operating System (ROS2 Humble). The USCA module sends the ultrasound image analysis results to the robot control module through the GET method of the HTTP protocol. The entire robotic system can operate stably at a frequency exceeding 10 Hz.

B. System Calibration

The coordinate systems and their transformations in the developed robotic system are also illustrated in Fig. 2(a). $\{RB\}$, $\{RE\}$, $\{C\}$, $\{US\}$ represent the robot base robot end flange, camera, and ultrasound image coordinate systems, respectively. $\{P\}$ represents the ultrasound probe coordinate system, its origin is located at the intersection of the central axis of the probe and the imaging surface, and its direction is consistent with the $\{RE\}$. The homogeneous transformation ${}^{RE}_{P}\boldsymbol{T} \in \mathrm{SE}(3)$ is obtained based on the geometry of the probe and its fixture. The transformation ${}^{RE}_{US}\boldsymbol{T} \in \mathrm{SE}(3)$ is obtained

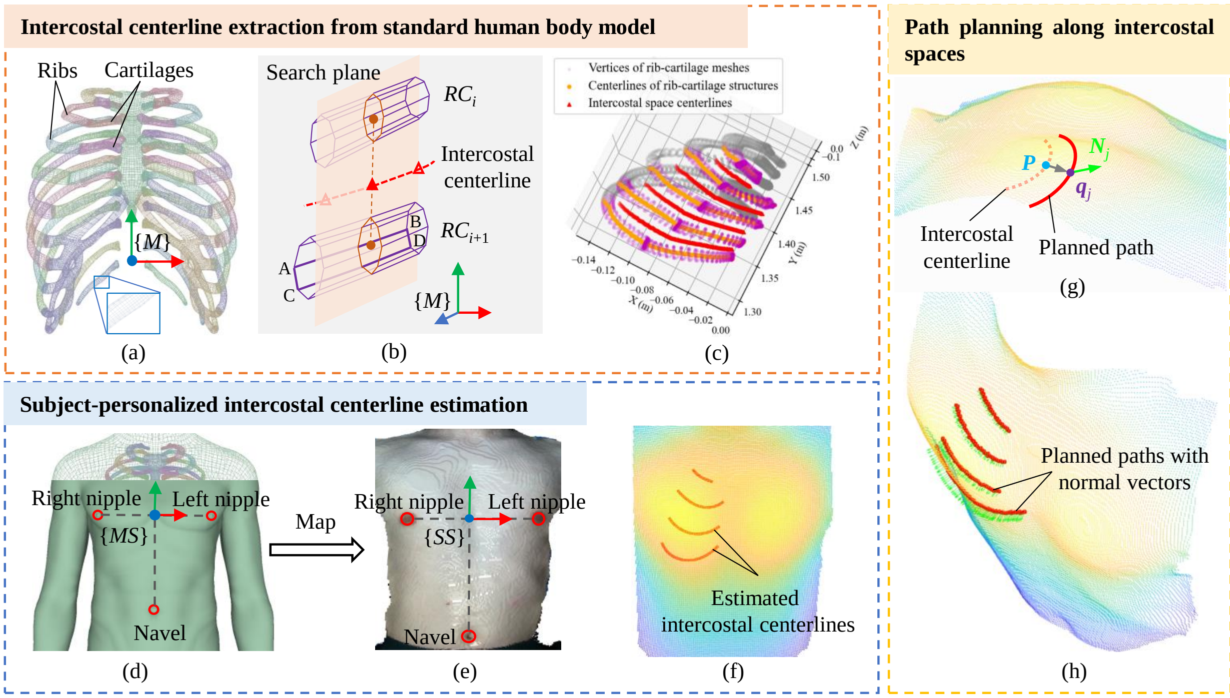

Fig. 3. Schematic diagram of longitudinal scan path planning method along the intercostal spaces. Starting from the (a) thorax skeleton framework of a standard human body model, the (b) plane-mesh intersection point search method is used to extract the (c) intercostal centerlines. Then, define the (d) human model skin frame and the (e) subject's skin frame using the nipples and the navel as landmarks, and map the intercostal centerlines extracted from the human model to the actual examined subject to estimate the (f) subject-personalized intercostal centerlines. Finally, a (g) normal vector matching method is used to project the estimated intercostal centerlines to the skin point cloud to obtain the (h) scan paths along the intercostal spaces.

by the ultrasound probe calibration using a N-wire phantom [36]. The transformation ${}^{RE}_{C}\boldsymbol{T} \in \mathrm{SE}(3)$ can be obtained by the eye-in-hand calibration with a calibration board [23], before which the camera is calibrated to obtain its internal parameters and align the RGB image with the depth image to provide accurate colorized point cloud of the subject's body surface. The transformation ${}^{RB}_{RE}\boldsymbol{T} \in \mathrm{SE}(3)$ is obtained by the robot forward kinematics. Based on these transformations, the subject's body surface point cloud can be mapped to the robot base coordinate system by the transformation

$$ {}^{RB}_{C}\boldsymbol{T} = {}^{RB}_{RE}\boldsymbol{T} \cdot {}^{RE}_{C}\boldsymbol{T}, \tag{1}$$

the subject's internal anatomy can be mapped to the robot base coordinate system by the transformation

$$ {}^{RB}_{US}\boldsymbol{T} = {}^{RB}_{RE}\boldsymbol{T} \cdot {}^{RE}_{US}\boldsymbol{T}, \tag{2}$$

and the target probe pose in the robot base coordinate system can be obtained by the transformation

$$ {}^{RB}_{P}\boldsymbol{T} = {}^{RB}_{RE}\boldsymbol{T} \cdot {}^{RE}_{P}\boldsymbol{T}. \tag{3}$$

The gravity compensation of the F/T sensor is performed by identifying the gravity and its center of the probe and fixture [37], to realize an accurate perception of the contact force/torque between the probe and the subject's skin.

IV. Longitudinal Scan Path Planning

In this paper, we propose an intercostal space centerline estimation method based on a standard human body model and the subject's body surface point cloud. On this basis, an ultrasound scanning path planning method along the intercostal spaces is developed. As shown in Fig. 3, we first extract the intercostal space centerlines from a standard human body model, then map the extracted intercostal space centerlines from the human body model to the subject according to the coordinate systems defined by the navel and nipples on body surface, and finally project them to the subject's body surface to complete the path planning along the intercostal spaces.

A. Intercostal Centerline Extraction from Standard Human Body Model

In this work, a standard adult male body model from the Zygote Body atlas (Zygote Media Group, Inc., American) is used. As shown in Fig. 3(a), this model includes skin and complete bony framework of thorax, in which each rib and its connected costal cartilage (CC) are individually represented as a polygonal mesh file mainly composed of a series of quadrilateral faces, such as Quadrilateral $ABCD$ in Fig. 3(b), where A, B, C, and D are its four vertices. Here, we merge the meshes of each rib and its adjacent costal cartilage, and refer to this combined structure as a rib-cartilage (RC) mesh. The origin of the human body model coordinate system $\{M\}$ is located on the midsagittal plane, with the X-axis pointing to the left, Y-axis to the inferior, and Z-axis to the anterior.

Based on the bony framework of thorax, the intercostal space centerlines are extracted using the **Algorithm** 1 as follows: Given adjacent rib-cartilage meshes, first, define a search plane parallel to the Y-O-Z plane of the coordinate system $\{M\}$, which moves from the middle to the sides of the

Algorithm 1: Intercostal Centerlines Extraction.

Input: Adjacent rib-cartilage meshes: $\{RC_i, i = 1, 2.\}$, left, right boundary and search interval distance of search plane: lb, rb, sd.
Output: Intercostal centerline: $centerline$.

```
// define function
Function ComputeSection(mesh, plane):
    section ← ∅;
    for face in mesh do
        for edge in face do
            if edge intersects plane then
                poins ← IntersectionPoint(edge, plane);
                Add point to section;
    return section.
// main algorithm
centerline ← ∅;
searchPlanes ← GenerateSearchPlanes(lb, rb, sd);
for plane in searchPlanes do
    section1 ← ComputeSection(RC1, plane);
    section2 ← ComputeSection(RC2, plane);
    if Length(section1) > 0 and Length(section2) > 0
    then
        center ← AveragePoints(section1 ∪ section2);
        Add center to centerline;
centerline ← Smooth(centerline);
return centerline.
```

body model at equal intervals. Then, at each search position, calculate the sections of rib-cartilage meshes intersected by this search plane. Next, determine the intercostal center by averaging the coordinates of these section points. By parameterization the intercostal centers across different positions of the search plane using cumulative chord lengths, and then fitting them using cubic B-splines, we ultimately obtain the smooth intercostal centerline. The extracted intercostal centerlines of the right chest are shown in Fig. 3(c).

B. Subject-personalized Intercostal Centerline Estimation

After extracting the intercostal space centerlines from the standard human body model, they need to be mapped onto the subject based on the body shape characteristics of the standard human body model and the subject, so as to obtain the subject's personalized intercostal space centerlines.

1) Body surface landmark positioning: Just like in the works [38], [39], we choose the nipples and navel on the skin surface as landmarks to describe the individual body shape. For the standard human body model, the positions of its nipple and navel centers are obtained by querying the corresponding vertex coordinates. For the subject, after obtaining the 2D RGB image, the image is first converted from the BGR color space to the HSV (Hue, Saturation, Value) color space, and the skin area is segmented by setting the HSV range of the skin color. Then, in order to improve the robustness of nipple and navel positioning under size uncertainty, a multi-scale template matching method is adopted. That is, the template image is scaled in multiple scales, the template matching is performed at each scale, and the result with the highest matching degree is selected as the target position. In particular, in order to eliminate the influence of brightness changes, the normalized cross-correlation (NCC) is used to measure the matching degree of the template image and the target image at the current position. Finally, according to the internal parameters of the camera, the landmarks detected in the RGB image are mapped to the point cloud data, and their positions in the camera coordinate system are obtained.

2) Skin coordinate system definition: Based on the detected body surface landmarks, the skin coordinate systems of the standard human body model and the subject, $\{MS\}$ and $\{SS\}$, are defined in the same way. As shown in 3(d-e), the origin of the skin coordinate system is set as the midpoint of the line connecting the two nipples, with the X-axis pointing from the right nipple to the left nipple, and the Y-axis pointing from the navel to the origin. For the human body model, since its skin is symmetrical and the plane where the navel and nipples are located is parallel to the X-O-Y plane of the coordinate system $M\}$, the model coordinate system $\{M\}$ and its skin coordinate system $\{MS\}$ have the same direction, with only an offset in the origin. For the subject, let ${}^{C}\boldsymbol{P}_{\mathrm{LN}} \in \mathbb{R}^3$, ${}^{C}\boldsymbol{P}_{\mathrm{RN}} \in \mathbb{R}^3$, and ${}^{C}\boldsymbol{P}_{\mathrm{NA}} \in \mathbb{R}^3$ respectively represent the positions of the centers of the left nipple, right nipple and navel in the camera coordinate system $\{C\}$, then, under the $\{C\}$, the origin of the coordinate system $\{SS\}$ can be obtained by

$$ {}^{C}\boldsymbol{O}_{SS} = ({}^{C}\boldsymbol{P}_{\mathrm{LN}} + {}^{C}\boldsymbol{P}_{\mathrm{RN}})/2, \tag{4} $$

the unit vector along the X-axis of the coordinate system $\{SS\}$ can be obtained by

$$ {}^{C}\boldsymbol{x}_{SS} = ({}^{C}\boldsymbol{P}_{\mathrm{LN}} - {}^{C}\boldsymbol{P}_{\mathrm{RN}})/\|{}^{C}\boldsymbol{P}_{\mathrm{LN}} - {}^{C}\boldsymbol{P}_{\mathrm{RN}}\|. \tag{5} $$

Taking into the landmark positioning errors, the unit vector along the Y-axis of the coordinate system $\{SS\}$ is obtained by

$$ {}^{C}\boldsymbol{y}_{SS} = \frac{{}^{C}\boldsymbol{y}_{SS}^{0} - ({}^{C}\boldsymbol{y}_{SS}^{0} \cdot {}^{C}\boldsymbol{x}_{SS}) \cdot {}^{C}\boldsymbol{x}_{SS}}{\|{}^{C}\boldsymbol{y}_{SS}^{0} - ({}^{C}\boldsymbol{y}_{SS}^{0} \cdot {}^{C}\boldsymbol{x}_{SS}) \cdot {}^{C}\boldsymbol{x}_{SS}\|}, \tag{6} $$

$$ {}^{C}\boldsymbol{y}_{SS}^{0} = {}^{C}\boldsymbol{O}_{SS} - {}^{C}\boldsymbol{P}_{\mathrm{NA}}. \tag{7} $$

Finally, the rotation transformation from the subject skin coordinate system to the camera coordinate system can be obtained by

$$ {}^{C}_{SS}\boldsymbol{R} = \left({}^{C}\boldsymbol{x}_{SS}, {}^{C}\boldsymbol{y}_{SS}, {}^{C}\boldsymbol{x}_{SS} \times {}^{C}\boldsymbol{x}_{SS}\right) \in \mathrm{SO}(3). \tag{8} $$

3) Mapping intercostal centerlins from standard human body model to subject: Due to the same coordinate system definition, the intercostal centerlines in the coordinate system $\{MS\}$ are mapped to the coordinate system $\{SS\}$ without rotation and translation transformations. Taking into account the body size difference between the actual subject and the standard human model, scaling is respectively performed in the X and Y directions during mapping, while the Z-axis coordinate remains unchanged. Let ${}^{M}\boldsymbol{P}_{\mathrm{LN}} \in \mathbb{R}^3$, ${}^{M}\boldsymbol{P}_{\mathrm{RN}} \in \mathbb{R}^3$, and ${}^{M}\boldsymbol{P}_{\mathrm{NA}} \in \mathbb{R}^3$ respectively represent the left nipple, right nipple and navel of the standard human body model, then, the scaling matrix from the human body model to the subject is calculated by

$$ {}^{SS}_{MS}\boldsymbol{D} = \begin{pmatrix} scaleX & 0 & 0 \\ 0 & scaleY & 0 \\ 0 & 0 & 1 \end{pmatrix}, \tag{9} $$

$$scaleX = \|^C\boldsymbol{P}_{\text{LN}} -^C \boldsymbol{P}_{\text{RN}}\|/\|^M\boldsymbol{P}_{\text{LN}} -^M \boldsymbol{P}_{\text{RN}}\|, \tag{10}$$

$$scaleY = \frac{\|^M\boldsymbol{O}_{MS} -^M \boldsymbol{P}_{\text{NA}}\|}{(^C\boldsymbol{O}_{SS} -^C \boldsymbol{P}_{\text{NA}}) \cdot^C \boldsymbol{y}_{SS}}, \tag{11}$$

$$^M\boldsymbol{O}_{MS} = (^M\boldsymbol{P}_{\text{LN}} +^M \boldsymbol{P}_{\text{RN}})/2. \tag{12}$$

Based on these transformations, the intercostal centerlines extracted from the thorax skeleton of the standard human model can be mapped to the camera coordinate system by (13) to finally estimate the subject's personalized intercostal centerlines, as shown in Fig. 3(f), which are combined with the subject's body surface point cloud data to provides a basis for scanning path planning along the intercostal spaces.

$$^C\boldsymbol{P}_{i,j} =^C_{SS} \boldsymbol{R} \cdot^{SS}_{MS} \boldsymbol{D} \cdot (^M\boldsymbol{P}_{i,j} -^M \boldsymbol{O}_{MS}) +^C \boldsymbol{O}_{SS} \tag{13}$$

where $^M\boldsymbol{P}_{i,j}$ is the j-th point on the i-th intercostal centerline extracted from the human body model, and $^C\boldsymbol{P}_{i,j}$ is its position mapped to the camera coordinate system.

C. Path Planning Along Intercostal Spaces

In order to obtain the ultrasound scanning paths along the intercostal spaces, a normal vector matching method is proposed to project the intercostal centerlines to the subject's body surface point cloud. Unlike conventional approaches that project 2D planar paths directly onto the surface of a 3D point cloud, our method takes into account the normal direction of the candidate points within the point cloud, thereby enhancing the accuracy of the planned paths along the intercostal spaces.

As shown in Fig. 3 (g), given an intercostal space point $\boldsymbol{P}$ and a body surface point cloud $\mathcal{Q}$, we first identify the point $\boldsymbol{q}_{\text{nearest}}$ in the point cloud that minimizes the distance to $\boldsymbol{P}$,

$$\boldsymbol{q}_{\text{nearest}} = \arg\min_{\boldsymbol{q}_i \in \mathcal{Q}} \|\boldsymbol{P} - \boldsymbol{q}_i\|, \tag{14}$$

next, etablish a neighborhood $\mathcal{N}$ around $\boldsymbol{q}_{\text{nearest}}$ with radius R,

$$\mathcal{N} = \{\boldsymbol{q}_j \in \mathcal{Q} \mid \|\boldsymbol{q}_j - \boldsymbol{q}_{\text{nearest}}\| \leq R\}, \tag{15}$$

finally, within the neighborhood, find the point $\boldsymbol{q}_{\text{target}}$ that maximizes the cosine of the angle between the vector to $\boldsymbol{P}$ and the normal vector $\boldsymbol{N}_j$,

$$\boldsymbol{q}_{\text{target}} = \arg\max_{\boldsymbol{q}_j \in \mathcal{N}} \frac{(\boldsymbol{P} - \boldsymbol{q}_j) \cdot \boldsymbol{N}_j}{\|\boldsymbol{P} - \boldsymbol{q}_j\|}, \tag{16}$$

thus, $\boldsymbol{q}_{\text{target}}$ is determined as the optimal projection point on the point cloud $\mathcal{Q}$.

Using this method, the candidate points along the entire trajectory are systematically identified, as shown in Fig. 3 (h), the proposed method successfully generates scan paths along the intercostal spaces.

V. Transverse Scan Path Planning and Online Probe Posture Adjustment

Due to the body shape difference between the subject and the standard human body model, the intercostal centerlines estimated in the previous section inevitably deviate from their true positions. As a result, the planned scanning path cannot completely follow the target intercostal spaces, this has a more significant impact on transverse scanning. Moreover, during the scanning process, the probe posture needs to be adjusted according to the actual pleural lines to fully expose the A-lines and B-lines that are meaningful for the diagnosis of lung diseases. To solve these problems, a transverse scan path planning method based on reconstructed intercostal centerlines, and an online probe posture adjustment method are proposed.

A. Pleural Line Segmentation

Accurate pleural line segmentation is the key to intercostal centerline reconstruction and online adjustment of probe posture. In this work, intercostal pleural line segmentation occurs in two scenarios: longitudinal scan and transverse scan. For the longitudinal scan, as shown in Fig. 4, scanning over the cartilages reveals the pleural lines beneath them due to their low acoustic impedance [28]. This results in a continuous high-echo line formed by the pleural line beneath the cartilage and the intercostal pleural line. Conversely, when scanning over the rib, the high acoustic impedance of the ribs causes posterior acoustic shadowing, making only the intercostal pleural line visible. This rib-pleura-rib structure creates the "bat sign". In this case, only the pleural line at the target intercostal space need to be precisely segmented while excluding the interference from the pleural lines beneath the cartilages and the pleural lines of adjacent intercostal spaces. For the transverse scan, as shown in Fig. 1, due to the absence of rib obstruction, the entire intercostal pleural line is continuously visible, and needs to be segmented.

To segment the specific pleural lines accurately in different scanning situations, we employ the nnU-Net framework [40]. Compared to other segmentation models that often require extensive manual parameter tuning, nnU-Net offers a robust and adaptable solution, automatically configuring itself to the specific dataset and task requirements, and has consistently achieved top performance in various medical image segmentation challenges. Specifically, the dataset comprises 1,168 images for training, including 508 from transverse scan and 660 from longitudinal scan. Additionally, 296 images are used for testing, consisting of 128 transversely scanned images and 168 longitudinally scanned images. All images were manually annotated accordingly by experienced clinicians.

All ultrasound images are with dimensions of 800 $\times$ 600 pixels, and they were normalized using Z-score method. Based on the nnU-Net framework, the U-Net structure with 6 down-sampling and 6 up-sampling layers was automatically configured. The training process utilized the Stochastic Gradient Descent (SGD) optimization algorithm with an initial learning rate of 0.01, a weight decay of 3×10^{-5}, and a momentum of 0.99 with Nesterov acceleration enabled. A polynomial learning rate scheduler was employed, adjusting the learning rate to facilitate efficient convergence. The experiments were conducted using an NVIDIA 2080 Ti GPU with 11 GB of memory. The model was trained for 1000 epochs, with each epoch consisting of 250 iterations. A batch size of 13 was employed during training to efficiently utilize the GPU resources and ensure stable convergence. The loss function combines Cross Entropy Loss and Dice Loss with equal weighting and incorporates deep supervision to encourage

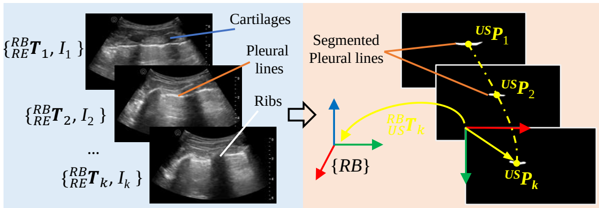

Fig. 4. Intercostal centerline reconstruction based on robot posture-segmented pleural line data from longitudinal scan, the yellow points represent the center points of the target intercostal pleural lines.

better feature learning throughout the model, enhancing segmentation performance.

B. Transverse Scan Path Planning Based on Intercostal Centerline Reconstruction

During the longitudinal scan, we save the center points of the target intercostal pleural lines in the ultrasound image coordinate system $\{^{US}\boldsymbol{P}_k | k = 1, ..., K\}$ and their corresponding coordinate transformations $\{^{RB}_{RE}\boldsymbol{T}_k | k = 1, ..., K\}$ to reconstruct the pleural centerline of the target intercostal space, which is regarded as the real target intercostal centerline. Considering the saving asynchrony between pleural line centroids and robot posture, we use timestamp alignment to get these paired data. Specifically, since the robot posture reading frequency is much higher than the ultrasound image processing, for each pleural line centroid, we search for the closest timestamp to its timestamp to get the corresponding robot posture. Then, the position of these centroids in the robot base coordinate system $\{RB\}$ can be obtained by

$$^{RB}\boldsymbol{P}_k = {}^{RB}_{RE}\boldsymbol{T}_k \cdot {}^{RE}_{US}\boldsymbol{T} \cdot {}^{US}\boldsymbol{P}_k, \tag{17}$$

and their position in the camera coordinate system $\{C\}$ can be further obtained by

$$^{C}\boldsymbol{P}_k = ({}^{RE}_{C}\boldsymbol{T})^{\mathrm{T}} \cdot ({}^{RB}_{RE}\boldsymbol{T}_{\mathrm{Cam}})^{\mathrm{T}} \cdot {}^{RB}\boldsymbol{P}_k, \tag{18}$$

where ${}^{RB}_{RE}\boldsymbol{T}_{\mathrm{Cam}}$ is the robot posture when obtaining the body surface point cloud by the RGB-D camera. Thus, the target intercostal centerline and the body surface point cloud are unified under one coordinate system.

On this basis, the reconstructed intercostal centerline is smoothed using the cubic B-spline fitting method based on cumulative chord length parameterization to avoid the interference of outlier points. Using the method in Section IV.*C*, a more accurate path along the intercostal space is obtained, when transverse scan along this path is performed, the obtained ultrasound images will not have rib shadows.

C. Online Adaptive Adjustments of Probe Posture

As shown in Fig. 5, there are two scenarios for online adaptive adjustment of the ultrasound probe posture, including the probe translation along its long axis (X-axis) to prevent the target pleural line from exceeding the field of view of the ultrasound image during longitudinal scans, and the rotation around its short axis (Y-axis) to visualize the diagnostically meaningful features, such as the A- and B-lines, during the whole scanning process, especially for transverse scan.

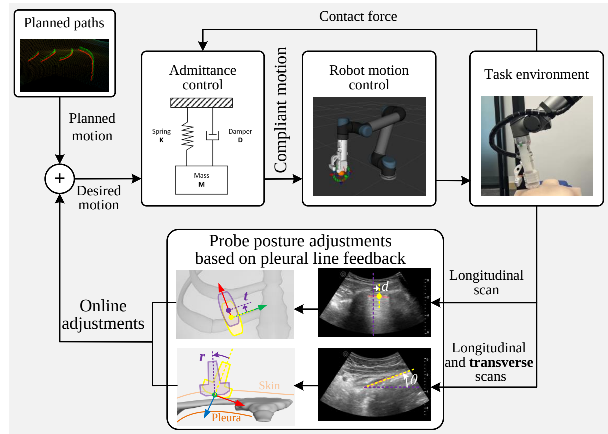

Fig. 5. General control scheme for autonomous robotic lung ultrasound scan.

1) Probe translation adjustment along its long axis: During our experiments, it was found that the estimated intercostal centerline is more accurate near the middle of the body, while the closer to the side of the body, the greater the deviation of the estimated intercostal centerline from the true position. This leads to the fact that during the scanning along a path planned based on the estimated inercostal centerline, the target intercostal pleural line is located in the middle of the ultrasound image area when the probe is placed close to the middle of the body, and then gradually deviates from the middle of the image area as the probe is moved to the side of the body, and finally may be out of the imaging field of view, resulting in incomplete target intercostal pleural line.

To maintain the target pleural line at the center of the image, we introduce an adaptive probe translation compensation method. Let d represent the center deviation of the target pleural line from the vertical centerline of the image. We introduce a threshold τ to determine the necessary probe movement, and the probe translation compensation t in its X-direction is given by

$$t = \begin{cases} d \cdot s, & \text{if } |d| > \tau, \\ 0, & \text{if } |d| \leq \tau, \end{cases} \tag{19}$$

where s is the isotropic pixel spacing of ultrasound images.

2) Probe rotation adjustment around its short axis: During lung ultrasound scan, it is necessary to ensure that the ultrasound waves are emitted perpendicularly to the pleura so as to adequately visualize the A- and B-lines and other signs that are meaningful for the diagnosis of lung diseases. To this end, we propose to use the pleural line in the directly observed ultrasound image as a feedback, and adjust the probe posture in real time to maintain the alignment of the pleural line with the horizontal axis of the image.

Let θ represent the angle deviation of the pleural line from the horizontal line of the image. We introduce an angular threshold ϕ to determine the necessary probe rotation, and the probe angle compensation r around its Y-axis is given by

$$r = \begin{cases} \theta, & \text{if } |\theta| > \phi, \\ 0, & \text{if } |\theta| \leq \phi. \end{cases} \tag{20}$$

D. Compliant Robot Motion Control

The ultrasound scanning procedure involves a significant amount of contact between the patient and the robot. Improper movement of the robot may result in excessive contact forces that could potentially injure the patient. To address this issue, we add an admittance controller to the robot's built-in motion controller. As shown in Fig. 5, after we obtain the desired motion from planned paths and online probe adjustments, we do not directly hand it over to the robot's motion controller for execution. Instead, we combine it with the measured contact force and admittance control law to calculate a compliant motion as the reference for the inner motion control loop. Although this may lead to imperfect execution of the desired motion, it allows the robot to automatically adjust its movement based on the contact force to avoid harming the patient.

In each control cycle, given the desired motion to be x_d, where $x_d \in \mathbb{R}^6$ representing the 6-DOF posture od the robot end-effector, i.e, the ultrasound probe. The compliant motion $x_c \in \mathbb{R}^6$ is determined by satisfying the following condition:

$$\mathcal{M}(\ddot{x}_c - \ddot{x}_d) + D(\dot{x}_c - \dot{x}_d) + K(x_c - x_d) = F_m - F_d \quad (21)$$

where $\mathcal{M}, D, K \in \mathbb{R}^{3\times3}$ are the virtual inertia, damping, and stiffness matrices, respectively. They can be fine-tuned according to desired robot dynamics. $F_m, F_d \in \mathbb{R}^6$ are the measured and desired 6-axis contact force-torque, respectively. F_d can be switched between 0 and non-zeros depending on whether on-purpose contact is wanted.

VI. Experiments and Results

A. Autonomous Robotic Lung Ultrasound Scan Workflow and Experimental Setups

A robotic automatic lung ultrasound scanning workflow is designed to closely replicate clinical physicians' scanning practices. After planning scanning paths along the intercostal spaces based on the estimated subject's personalized intercostal centerlines, the robot scans each intercostal space one by one. For each intercostal space, the longitudinal scan is first conducted, and the robot moves the probe from the middle of the body to the side along the planned path. During the scanning, the target pleural lines are segmented from real-time ultrasound images, and probe translation adjustment along its long axis is performed based on the center deviation of the target pleural line. Additionally, the center points of the target intercostal pleural lines in the ultrasound images along with the corresponding robot poses are saved in pairs. At the end of the longitudinal scan, the actual intercostal centerline is reconstructed, and the scanning path is replanned for the following transverse scan. Then, the transverse scan is conducted from the side to the middle of the human body. During this process, the probe rotation adjustment around its short axis is performed based on the angle deviation of the pleural line. In this way, diagnostically meaningful ultrasound images with as few rib shadows as possible can be obtained.

As shown in Fig. 6, in order to ensure the safety of autonomous robotic lung ultrasound scanning, we first verified the compliant motion control method on a chest phantom. On this premise, we conducted experimental evaluations of the path planning methods, probe adjustment methods, and overall system performance on the anterior chest of a volunteer.

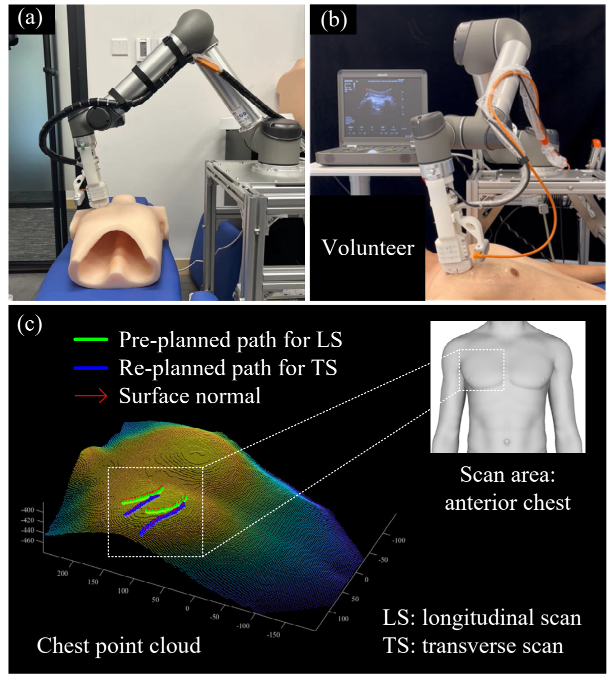

Fig. 6. Experimental setups, including the compliant motion control experiment on (a) a chest phantom, and extensive experiments on (b) the anterior chest of a volunteer to evaluate (c) path planning methods, probe posture adjustment methods, and overall system performance.

B. Performance of Compliant Motion Control

For the phantom experiment, after obtaining the surface point cloud of the phantom by the RGB-D camera, a scanning path was planned on its right chest surface. Along this path, the longitudinal scan was first conducted from the middle to the side of the phantom, and then the transverse scan was performed from the side back to the starting position. In each scan, the probe stayed in place for 4 s when locating the initial position and arriving at the end point, and the intermediate scanning time was 30 s. We performed the experiments with and without the compliant motion control, and the contact force in Z-direction was recorded at 100 Hz.

As shown in Fig. 7, when compliant motion control was not enabled, during the longitudinal scan process, once the probe contacted the phantom, F_z increased sharply to nearly 60 N. As the probe moved, the contact force gradually decreased. In the latter part of the path, the contact force dropped to 0, indicating that the probe has lost contact with the phantom surface. Conversely, during the transverse scan process, the contact force started at 0 and gradually increased to over 40 N. After enabling compliant motion control, during the longitudinal scan, when the probe contacted the phantom, F_z increased rapidly but did not exceed 13 N at its maximum. This is because force control was only enabled in the Z-direction of the probe, while other directions remained stationary at this time. When the probe began to move, the F_z stabilized around the set value of 8 N. When the probe reached the end of the

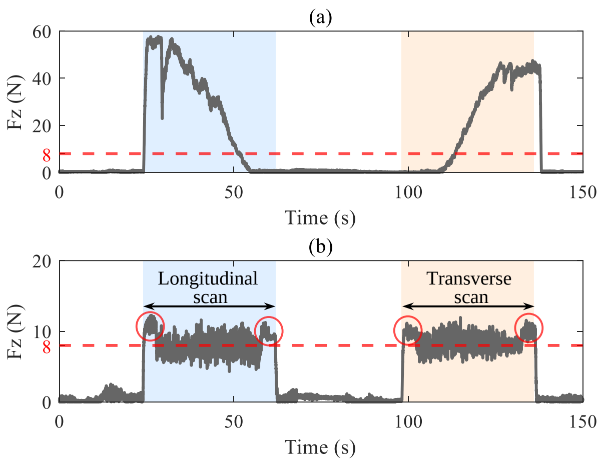

Fig. 7. Contact forces in Z-direction during scanning on a chest phantom (a) without compliant motion control, and (b) with compliant motion control. In (b), the red circle corresponds to the force when the probe remains stationary in other directions except the Z-direction.

path and remained stationary except for the Z-direction, F_z experienced a brief, slight increase. During the transverse scan process, F_z behaved similarly. The experimental results clearly demonstrate that using the compliant motion control ensures stable contact between the probe and the skin while avoiding excessive contact force that could harm the subject.

C. Pleural Line Segmentation Results

To evaluate the pleural line segmentation model's performance on the test set, four metrics are adopted. Among them, dice coefficient indicates the overlap between the predicted and true segmentation, 95th percentile Hausdorff distance (HD95) measures the distance between two boundaries while reducing sensitivity to outliers. Average surface distance (ASD) calculates the average distance between the surfaces of the segmented and ground truth regions. Jaccard index (JC), also known as intersection over union (IoU), is similar to Dice, but penalizes disjoint sets more heavily. These metrics provide a comprehensive assessment of segmentation quality. The results of the pleural line segmentation in two scanning scenarios, longitudinal scan and transverse scan, are shown in Table I. Overall, these results suggest the model performs well in the both scenarios, with good overlap and boundary accuracy. The segmentation results in the case of transverse scan are slightly worse than those in the case of longitudinal scan because the visible pleural line tends to be thin and long in the transverse scan scenario, and its accurate segmentation is more likely to be disturbed by the surrounding tissue, as shown in Fig. 8.

TABLE I
PLEURAL LINE SEGMENTATION RESULTS ON THE TEST SET IN TERMS OF MEAN VALUES OF FOUR QUANTITATIVE METRICS. ↑ / ↓ INDICATES THE HIGHER/LOWER THE SCORE, THE BETTER.

Scenarios	Dice (%)↑	HD95 (pixel)↓	ASD (pixel)↓	JC (%)↑
Transverse	85.08	3.25	1.37	74.13
Longitudinal	86.17	3.24	1.26	76.18

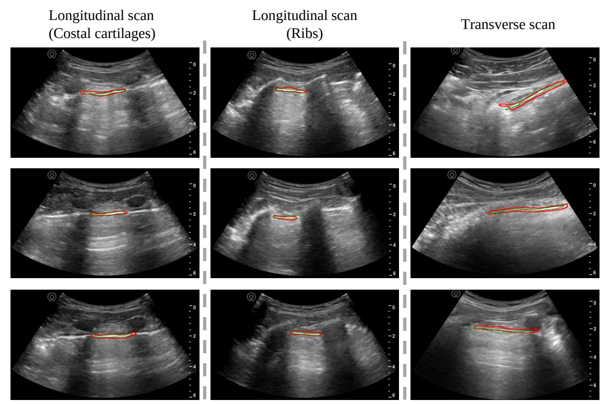

Fig. 8. Sample segmentation results in three cases. Segmented and ground truth region boundaries are shown by red and green contours, respectively.

D. Pre-scan Path Planning & Intra-scan Path Replanning

In order to verify the validity of the pre-scan path planning method and the intra-scan path replanning method, we conducted robotic ultrasound scanning experiments on a volunteer in the form of longitudinal scan along the paths planned according to the two methods, respectively, as shown in Fig. 6(c). In the experiments, the probe was moved from the middle to the side of the body. During the scanning process, the center deviations of the target intercostal pleural lines as well as the ultrasound images were recorded to characterize the accuracy of the paths along the intercostal spaces.

As shown in Fig. 9, during the scanning following the pre-planned path, the center deviation of the target intercostal pleural line was within the desired range [-5, 5] (mm) when the probe was positioned near the middle of the body. As the probe was gradually moved to the lateral part of the body, the target intercostal pleural line gradually deviated from the center of the image, and finally the degree of deviation leveled off, with a maximum deviation magnitude of more than 17 mm throughout the scan. However, as shown in the ultrasound images Fig. 9 (b1)-(b4) at the four time nodes (0, 10, 20, 30) (s), corresponding to the center deviations of (-4.01, -12.78, -16.01, -16.02) (mm), the target intercostal pleural lines were completely visible in the ultrasound images throughout the scanning, confirming the effectiveness of the pre-scan path planning method for longitudinal scan. During the scanning following the re-planned path, the center deviation values of the target intercostal pleural line were remained within the desired range, and the target intercostal pleural lines were almost in the middle of the ultrasound images, just as in images Fig. 9 (d1)-(d4) at the four time nodes, where the corresponding center deviations are 1.18 mm, 1.71 mm, 2.04 mm, and 2.10 mm, respectively. The result indicates that the intra-scan replanned path based on the reconstructed target intercostal pleural centerline can effectively ensure that the probe scans along the actual intercostal centerline, thus ensuring that the obtained images are not obstructed by ribs during transverse scan.

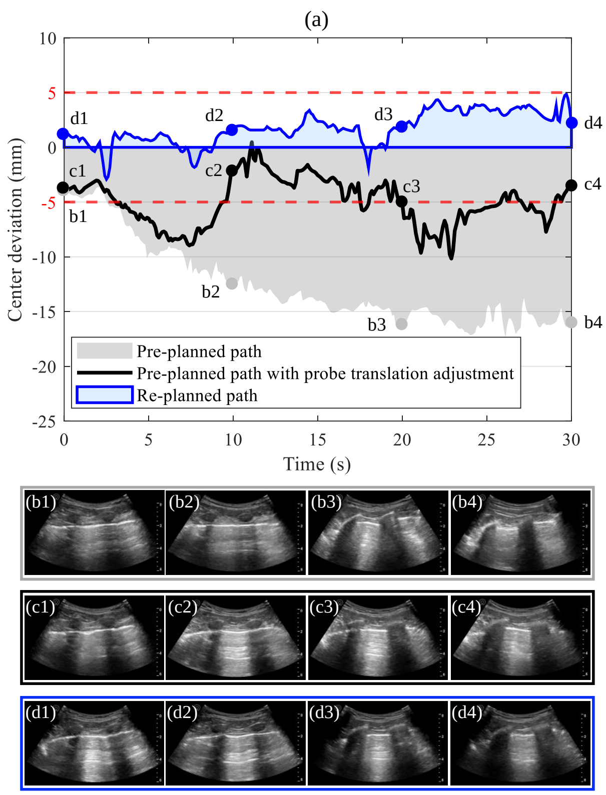

Fig. 9. Experimental results on the effectiveness of pre-scan path planning, intra-scan path replanning, and online probe translation adjustment methods.

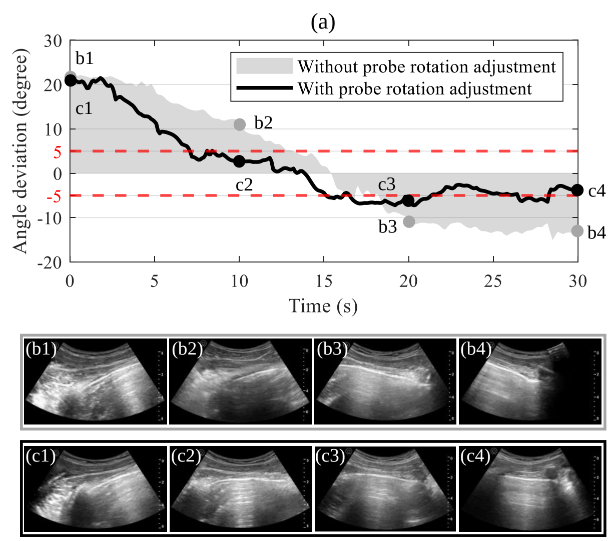

Fig. 10. Experimental results on the effectiveness of online probe rotation adjustment methods.

E. Online Adaptive Adjustments of Probe Posture

1) Translation adjustment of the probe along its long axis: In order to evaluate the effectiveness of the online probe translation adjustment method, the online probe translation adjustment function was enabled during the robotic ultrasound scanning along the pre-planned path, and the comparative experimental results with and without the online probe translation adjustment are also shown in Fig. 9. As can be seen from the figure, starting from the same initial position, the center deviation of the target intercostal pleural line fluctuated around the -5 mm line as the probe traveled to the lateral part of the body with the probe translation adjustment, with a minimum value of -10.16 mm, rather than decreasing all the way below -17 mm as it would have done without the probe translation adjustment. As shown in the ultrasound images at the four time points (0, 10, 20, 30) (s), the target intercostal pleural line always remained in the middle of the image in the presence of the probe translation adjustment, which not only facilitates the diagnosis of the disease based on the image obtained from the scanning, but also avoids the target intercostal pleural line from exceeding the imaging range, thus guaranteeing the reconstruction accuracy of the target intercostal centerline to further replan the path for the following transverse scan.

2) Rotation adjustment of the probe around its short axis: In order to verify the effectiveness of the online probe rotation adjustment method, we compared the angle deviation of the intercostal pleural line and the obtained ultrasound images during transverse scan with and without the probe rotation adjustment along the re-planned path, with the probe moving from the lateral side of the body to the middle part of the body, as shown in Fig. 10. As can be seen from the figure, when without the online probe rotation adjustment, the absolute values of the pleural line angle deviations were larger when the probe was located near the side and middle of the body, and the maximum value exceeded 22°, revealing the fact that determining the probe posture according to the normal vector of the body surface was not sufficient to ensure that the ultrasound waves were vertically incident on the lungs.

Starting from the same initial angle deviation, when with the probe rotation adjustment, the angle deviation was adjusted to below 5°at a significant rate and eventually fluctuated around the -5°. By comparing the ultrasound images at the four time points (0, 10, 20, 30) (s), (b1-b4) corresponded to angle deviations of 21.34°, 2.58°, -6.12°, and -3.33°, respectively, and (c1-c4) corresponded to angular deviations of 21.83°, 11.66°, -10.06°, and -11.40°, respectively. It can be seen that the pleural line stabilized near the horizontal position of the images for a longer period of time in the presence of online probe rotation, and the A-line was also more clearly visualized in this case. These results demonstrate the necessity of online probe rotation adjustment based on pleural line angle deviation and its effectiveness in obtaining diagnostically meaningful ultrasound images.

F. Performance of Robotic Lung Ultrasound Scan System

Based on the aforementioned method verification, we conducted a complete robotic autonomous lung ultrasound scanning experiment according to the workflow described in Section VI.*A*, that is, first performed a longitudinal scan, and then performed a transverse scan, and adjusted the probe posture while scanning. The key frames during the scanning process are shown in Fig. 11. The experimental results show that the entire scanning process meets the expected results. We also showed the Z-axis contact force F_z, as in Fig. 11(b). It can

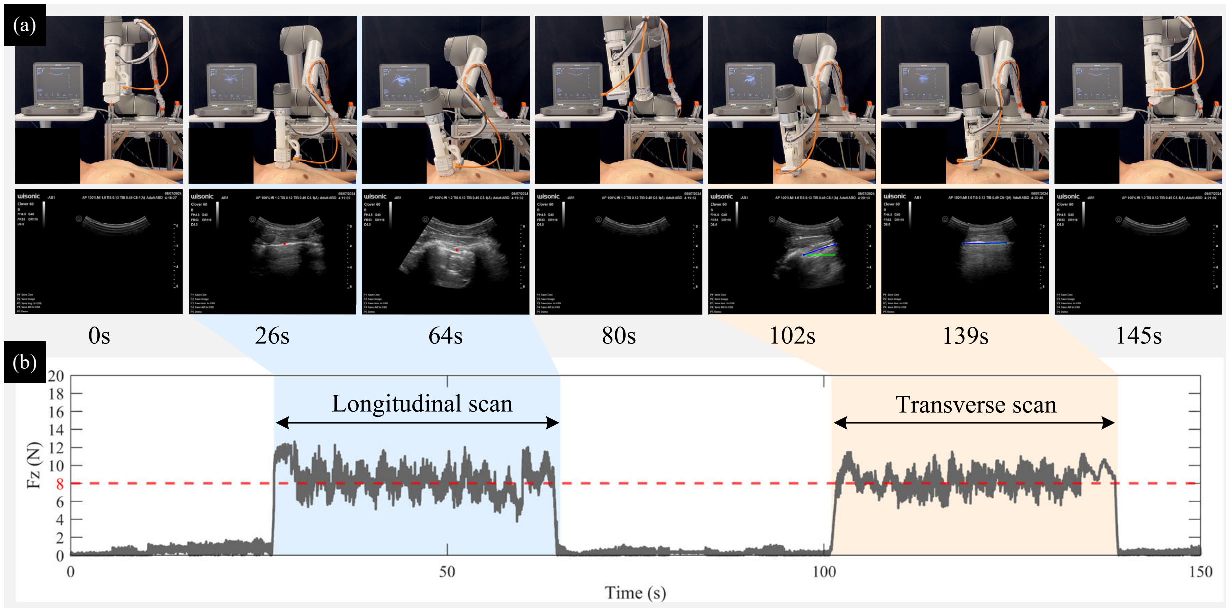

Fig. 11. Visualization of (a) robotic lung ultrasound scan process along one intercostal space of the volunteer, as well as the (b) contact force in Z-direction. In (a), the red point in the ultrasound images is the center of the target intercostal pleural line during longitudinal scan, and the blue line connecting the two endpoints of the pleural line relative to the horizontal green line indicates the inclination of the probe relative to the pleura during transverse scan.

be seen that the F_z behaved the same way on the volunteer as it did on the chest phantom, confirming the safety of the robotic ultrasound scan on human body.

VII. Conclusion

In this paper, we addressed key challenges in achieving autonomous lung ultrasound scans. We proposed a novel method for longitudinal and transverse scan path planning along intercostal spaces, coupled with ultrasound probe posture control based on pleural line feedback from images. Additionally, we developed a robotic lung ultrasound system and validated the effectiveness of our proposed methods in obtaining diagnostically meaningful ultrasound images on a volunteer. Currently, our work focuses solely on the anterior chest region, where we achieved successful results. In future work, we will extend and refine these methods to enable autonomous robotic ultrasound scanning of the entire lung area. This advancement aims to relieve doctors from intensive and potentially infectious manual procedures, ultimately benefiting both medical professionals and patients.

References

[1] A. Saraogi, "Lung ultrasound: Present and future," *Lung India*, vol. 32, no. 3, pp. 250–257, 2015.

[2] I. Blazic, C. Cogliati, N. Flor, G. Frija, M. Kawooya, M. Umbrello, S. Ali, M.-L. Baranne, Y.-J. Cho, R. Pitcher, *et al.*, "The use of lung ultrasound in covid-19," *ERJ Open Research*, vol. 9, no. 1, 2023.

[3] T. J. Marini, B. Castaneda, T. Baran, T. P. O'Connor, B. Garra, L. Tamayo, M. Zambrano, C. Carlotto, L. Trujillo, and K. A. Kaproth-Joslin, "Lung ultrasound volume sweep imaging for pneumonia detection in rural areas: piloting training in rural peru," *Journal of clinical imaging science*, vol. 9, 2019.

[4] F. Mojoli, B. Bouhemad, S. Mongodi, and D. Lichtenstein, "Lung ultrasound for critically ill patients," *American journal of respiratory and critical care medicine*, vol. 199, no. 6, pp. 701–714, 2019.

[5] T. J. Marini, D. J. Rubens, Y. T. Zhao, J. Weis, T. P. O'connor, W. H. Novak, and K. A. Kaproth-Joslin, "Lung ultrasound: the essentials," *Radiology: Cardiothoracic Imaging*, vol. 3, no. 2, p. e200564, 2021.

[6] G. Soldati, M. Demi, A. Smargiassi, R. Inchingolo, and L. Demi, "The role of ultrasound lung artifacts in the diagnosis of respiratory diseases," *Expert review of respiratory medicine*, vol. 13, no. 2, pp. 163–172, 2019.

[7] S. Abbas and P. Peng, "Basic principles and physics of ultrasound," *Ultrasound for Interventional Pain Management: An Illustrated Procedural Guide*, pp. 1–31, 2020.

[8] J. Wang, X. Yang, B. Zhou, J. J. Sohn, J. Zhou, J. T. Jacob, K. A. Higgins, J. D. Bradley, and T. Liu, "Review of machine learning in lung ultrasound in covid-19 pandemic," *Journal of Imaging*, vol. 8, no. 3, p. 65, 2022.

[9] L. Gargani and G. Volpicelli, "How i do it: lung ultrasound," *Cardiovascular ultrasound*, vol. 12, pp. 1–10, 2014.

[10] K. Li, Y. Xu, and M. Q.-H. Meng, "An overview of systems and techniques for autonomous robotic ultrasound acquisitions," *IEEE Transactions on Medical Robotics and Bionics*, vol. 3, no. 2, pp. 510–524, 2021.

[11] Z. Jiang, S. E. Salcudean, and N. Navab, "Robotic ultrasound imaging: State-of-the-art and future perspectives," *Medical image analysis*, p. 102878, 2023.

[12] X. Ma, Z. Zhang, and H. K. Zhang, "Autonomous scanning target localization for robotic lung ultrasound imaging," in *2021 IEEE/RSJ International Conference on Intelligent Robots and Systems (IROS)*, pp. 9467–9474, IEEE, 2021.

[13] L. Al-Zogbi, V. Singh, B. Teixeira, A. Ahuja, P. S. Bagherzadeh, A. Kapoor, H. Saeidi, T. Fleiter, and A. Krieger, "Autonomous robotic point-of-care ultrasound imaging for monitoring of covid-19–induced pulmonary diseases," *Frontiers in Robotics and AI*, vol. 8, p. 645756, 2021.

[14] B. Zhang, K. Xu, H. Cong, and M. Sun, "Channel and spatial attention mechanism-based yolo network for target detection of the lung ultrasound scanning robot," in *2023 9th International Conference on Control Science and Systems Engineering (ICCSSE)*, pp. 319–324, IEEE, 2023.

[15] B. Zhang, H. Cong, Y. Shen, and M. Sun, "Visual perception and convolutional neural network based robotic autonomous lung ultrasound scanning localization system," *IEEE Transactions on Ultrasonics, Ferroelectrics, and Frequency Control*, 2023.

[16] F. Suligoj, C. M. Heunis, J. Sikorski, and S. Misra, "Robust–an autonomous robotic ultrasound system for medical imaging," *IEEE access*, vol. 9, pp. 67456–67465, 2021.

[17] X. Ma, W.-Y. Kuo, K. Yang, A. Rahaman, and H. K. Zhang, "A-see: Active-sensing end-effector enabled probe self-normal-positioning for

robotic ultrasound imaging applications," *IEEE robotics and automation letters*, vol. 7, no. 4, pp. 12475–12482, 2022.

[18] J. Tan, B. Li, Y. Leng, Y. Li, J. Peng, J. Wu, B. Luo, X. Chen, Y. Rong, and C. Fu, "Fully automatic dual-probe lung ultrasound scanning robot for screening triage," *IEEE Transactions on Ultrasonics, Ferroelectrics, and Frequency Control*, 2022.

[19] M. Blaivas, "Lung ultrasound in evaluation of pneumonia," *Journal of Ultrasound in Medicine*, vol. 31, no. 6, pp. 823–826, 2012.

[20] D. A. Lichtenstein, "Blue-protocol and falls-protocol: two applications of lung ultrasound in the critically ill," *Chest*, vol. 147, no. 6, pp. 1659–1670, 2015.

[21] X. Wang, D. Liu, H. Zhang, H. He, Y. Liu, W. Chai, and W. Du, "The value of bedside lung ultrasound in emergency-plus protocol for the assessment of lung consolidation and atelectasis in critical patients," *Zhonghua nei ke za zhi*, vol. 51, no. 12, pp. 948–951, 2012.

[22] J. M. Smit, M. E. Haaksma, M. H. Winkler, M. L. Heldeweg, L. Arts, E. J. Lust, P. W. Elbers, L. J. Meijboom, A. R. Girbes, L. M. Heunks, *et al.*, "Lung ultrasound in a tertiary intensive care unit population: a diagnostic accuracy study," *Critical Care*, vol. 25, pp. 1–9, 2021.

[23] Z. Wang, B. Zhao, P. Zhang, L. Yao, Q. Wang, B. Li, M. Q.-H. Meng, and Y. Hu, "Full-coverage path planning and stable interaction control for automated robotic breast ultrasound scanning," *IEEE Transactions on Industrial Electronics*, vol. 70, no. 7, pp. 7051–7061, 2022.

[24] Q. Huang, J. Lan, and X. Li, "Robotic arm based automatic ultrasound scanning for three-dimensional imaging," *IEEE Transactions on Industrial Informatics*, vol. 15, no. 2, pp. 1173–1182, 2018.

[25] K. Okuzaki, N. Koizumi, K. Yoshinaka, Y. Nishiyama, J. Zhou, and R. Tsumura, "Rib region detection for scanning path planning for fully automated robotic abdominal ultrasonography," *International Journal of Computer Assisted Radiology and Surgery*, vol. 19, no. 3, pp. 449–457, 2024.

[26] C. Graumann, B. Fuerst, C. Hennersperger, F. Bork, and N. Navab, "Robotic ultrasound trajectory planning for volume of interest coverage," in *2016 IEEE international conference on robotics and automation (ICRA)*, pp. 736–741, IEEE, 2016.

[27] Y. Bi, C. Qian, Z. Zhang, N. Navab, and Z. Jiang, "Autonomous path planning for intercostal robotic ultrasound imaging using reinforcement learning," *arXiv preprint arXiv:2404.09927*, 2024.

[28] Z. Jiang, C. Li, X. Lil, and N. Navab, "Thoracic cartilage ultrasound-ct registration using dense skeleton graph," in *2023 IEEE/RSJ International Conference on Intelligent Robots and Systems (IROS)*, pp. 6586–6592, IEEE, 2023.

[29] C. Yang, M. Jiang, M. Chen, M. Fu, J. Li, and Q. Huang, "Automatic 3-d imaging and measurement of human spines with a robotic ultrasound system," *IEEE Transactions on Instrumentation and Measurement*, vol. 70, pp. 1–13, 2021.

[30] Z. Jiang, M. Grimm, M. Zhou, J. Esteban, W. Simson, G. Zahnd, and N. Navab, "Automatic normal positioning of robotic ultrasound probe based only on confidence map optimization and force measurement," *IEEE Robotics and Automation Letters*, vol. 5, no. 2, pp. 1342–1349, 2020.

[31] Z. Jiang, M. Grimm, M. Zhou, Y. Hu, J. Esteban, and N. Navab, "Automatic force-based probe positioning for precise robotic ultrasound acquisition," *IEEE Transactions on Industrial Electronics*, vol. 68, no. 11, pp. 11200–11211, 2020.

[32] G. Ning, H. Liang, X. Zhang, and H. Liao, "Autonomous robotic ultrasound vascular imaging system with decoupled control strategy for external-vision-free environments," *IEEE Transactions on Biomedical Engineering*, 2023.

[33] B. Ihnatsenka and A. P. Boezaart, "Ultrasound: Basic understanding and learning the language," *International journal of shoulder surgery*, vol. 4, no. 3, p. 55, 2010.

[34] Z. Jiang, Z. Li, M. Grimm, M. Zhou, M. Esposito, W. Wein, W. Stechele, T. Wendler, and N. Navab, "Autonomous robotic screening of tubular structures based only on real-time ultrasound imaging feedback," *IEEE Transactions on Industrial Electronics*, vol. 69, no. 7, pp. 7064–7075, 2021.

[35] G. Faoro, S. Maglio, S. Pane, V. Iacovacci, and A. Menciassi, "An artificial intelligence-aided robotic platform for ultrasound-guided transcarotid revascularization," *IEEE Robotics and Automation Letters*, vol. 8, no. 4, pp. 2349–2356, 2023.

[36] L. Lei, B. Zhao, X. Qi, R. Mi, H. Ye, P. Zhang, Q. Wang, P.-A. Heng, and Y. Hu, "Robotic needle insertion with 2d ultrasound–3d ct fusion guidance," *IEEE Transactions on Automation Science and Engineering*, 2023.

[37] Y. Yu, R. Shi, and Y. Lou, "Bias estimation and gravity compensation for wrist-mounted force/torque sensor," *IEEE Sensors Journal*, vol. 22, no. 18, pp. 17625–17634, 2021.

[38] A. S. B. Mustafa, T. Ishii, Y. Matsunaga, R. Nakadate, H. Ishii, K. Ogawa, A. Saito, M. Sugawara, K. Niki, and A. Takanishi, "Development of robotic system for autonomous liver screening using ultrasound scanning device," in *2013 IEEE international conference on robotics and biomimetics (ROBIO)*, pp. 804–809, IEEE, 2013.

[39] R. Tsumura, Y. Koseki, N. Nitta, and K. Yoshinaka, "Towards fully automated robotic platform for remote auscultation," *The International Journal of Medical Robotics and Computer Assisted Surgery*, vol. 19, no. 1, p. e2461, 2023.

[40] F. Isensee, P. F. Jaeger, S. A. Kohl, J. Petersen, and K. H. Maier-Hein, "nnu-net: a self-configuring method for deep learning-based biomedical image segmentation," *Nature methods*, vol. 18, no. 2, pp. 203–211, 2021.